AIMS Energy, 12(5): 1075–1095.
DOI: 10.3934/energy.2024051
Received: 29 June 2024
Revised: 03 October 2024
Accepted: 15 October 2024
Published: 24 October 2024

https://www.aimspress.com/journal/energy

Research article

Optimization of hybrid photovoltaic-thermal systems integrated into buildings: Impact of bi-fluid exchangers and filling gases on the thermal and electrical performances of solar cells

Kokou Aménuvéla Toka[1,*], Yawovi Nougblégа[1,2,*] and Komi Apélété Amou[1,2]

[1] Solar Energy Laboratory, Department of Physics, Faculty of Sciences, University of Lomé, Togo
[2] Regional Center of Excellence for Electricity Management (CERME), University of Lomé, Togo

* **Correspondence:** Email: tokakokou@gmail.com, nycogl@yahoo.fr; Tel: +22890218796.

Abstract: The low cooling efficiency of photovoltaic panels integrated into building façades restricts their electrical performance. The innovative approach of a dual-fluid photovoltaic-thermal system (BFPVT), incorporating bi-fluid cooling exchangers, appears to be a promising solution for jointly optimizing the electrical and thermal performance of PVT systems. However, despite the introduction of air heat shields to improve this performance, their limited efficiency makes them less competitive. We present a photovoltaic-thermal (PVT) system with a two-channel heat exchanger. The upper channel contains a stagnant fluid, which acts as a heat shield, while the lower, open channel ensures the continuous circulation or evacuation of heat transfer air. A copper metal plate separates the two channels. We examined the impact of various fluids employed as heat shields, including neon, argon, and xenon, in comparison to air, on the thermal and electrical performance of the collector. We employed numerical modeling of convective and conductive transfers to assess the average thermal efficiency of the BFPVT and the rise in PV temperature in the analyzed configuration. The equations were discretized using the implicit finite difference method and solved using the Thomas and Gauss-Seidel algorithms. The results demonstrated an 18% enhancement in thermal efficiency with the utilization of neon. In contrast, the employment of argon and xenon markedly reduced the mean temperature of photovoltaic cells by 4.82 °C and 4.87 °C, respectively. This led to an increase in their electrical efficiency by 0.33% in comparison to air. Thus, argon is regarded as the optimal choice for optimizing electrical efficiency, taking into account both economic and environmental considerations.

Keywords: numerical study; photovoltaic/thermal panels; bi-fluid collector; mixed convection; thermoelectric performance

Nomenclature: Letters: A: Aspect ratio dimensionless of the global system ($A = \frac{H}{L}$); a_r: Relative thermal diffusivity ($a_r = \frac{\lambda_r}{\rho_r Cp_r}$); B_1: Aspect ratio between the width of the enclosed fluid gap and the length of the collector ($B_1 = \frac{e_{f1}}{L}$); B_{i1}: Biot number of the enclosed fluid1 ($B_{i1} = \frac{h_{f1}L}{\lambda_S}$); B_{i2}: Biot number of the air ($B_{i2} = \frac{h_{f2}L}{\lambda_S}$); Cp: Specific heat (J. Kg^{-1}. K^{-1}); $ef1$: Width of enclosed fluid gap (m); $ef2$: Airflow duct width (m); e_S: Thickness of metal plate (m); g: Gravity acceleration (m.s^{-2}); h: Convective transfer coefficient (W m^{-2}K^{-1}); H: Height of collector (m); L: Length of collector (m); Ra: Rayleigh number ($Ra = \frac{\rho^2 g\beta\emptyset L^4}{\lambda\mu^2}$); Pr: Prandtl number ($Pr = \frac{\mu c_p}{\lambda}$); Re: Reynolds number ($Re = \frac{\rho V_0 L}{\mu}$); t: Temps (s); T: Temperature (K); T_a: Ambient air temperature (K); u, v: Velocity components in x and y directions (m.s^{-1}); U, V: Dimensional components of velocity in X and Y directions ($U = \frac{u}{v_0}$; $V = \frac{v}{v_0}$); v_0: Air inlet velocity in the lower channel of the chimney (m.s^{-1}); X, Y: Dimensionless Cartesian coordinates ($X = \frac{x}{L}$; $Y = \frac{y}{L}$); x, y: Cartesian coordinates (m);
Greek letters: β: Coefficient of thermal expansion (K^{-1}); Ω: Dimensionless vorticity ($\Omega = \frac{\omega v_0}{L}$); ω: Dimensional vorticity (s^{-1}); ψ: Dimensional stream function (m^2.s^{-1}); Ψ: Dimensionless stream function ($\Psi = \frac{\psi}{Lv_0}$); Θ: Dimensionless temperature ($\theta = \lambda\left(\frac{T-T_a}{\phi L}\right)$); τ: Dimensionless time ($\tau = \frac{v_0}{L}t$); λ: Thermal Conductivity Coefficient (W.m^{-1}. K^{-1}); μ: Air dynamic viscosity (Kg.m^{-1}. s^{-1}); ρ: Air density (Kg.m^{-3}); τ: Transmission coefficient (-); η_{el}: Electrical efficiency of PV cells (-); η_{th}: Thermal efficiency of PV cells (-); Φ: Solar flux density (W.m^{-2});
Indices: f_1: Fluid 1; f_2: Fluid 2; S: Solid; pv: Photovoltaic; r: Relative

1. Introduction

In the current energy context, reducing energy consumption in the residential sector is crucial, as it is a major energy consumer [1]. One of the most effective strategies for improving thermal efficiency and utilizing renewable energy is incorporating photovoltaic components into buildings [2,3]. Marei et al. [4] investigated and compared the energy-saving capabilities of four transparent building wall configurations: Basic glass, facade, basic glass integrated with photovoltaic panels, and facades integrated with photovoltaic panels. The researchers considered different ambient temperatures, wind velocities, and solar radiation levels. The findings show that the facade, photovoltaic-integrated basic glass, and photovoltaic-integrated facade configurations reduced 46.9%, 31.5%, and 79.3% in total electricity consumption compared to the basic glass wall. The efficiency of a novel solar photovoltaic thermoelectric air conditioner (SPVTEAC) for local air conditioning of a 1 m³ compartment was evaluated through experimental investigation under a range of indoor cooling loads by Mohamed et al. [5]. Their results indicated that the SPVTEAC could maintain an average daily air compartment temperature of 27.50 °C. Building Integrated Photovoltaic (BIPV) systems offer high performance for next-generation green buildings [6]. However, one challenge associated with integration is the overheating of photovoltaic cells, causing a loss of efficiency and accelerated deterioration. In a study conducted by Krauter et al. [7], it was found that solar cell overheating is a significant issue for building-integrated

PV panels, leading to a notable reduction in electrical efficiency of almost 9%. Photovoltaic (PV) panels can convert between 5% and 20% of incident solar irradiation into electricity [8,9], with the remaining absorbed irradiation transformed into waste heat [8,10]. The accumulation of waste heat causes the photovoltaic cells to overheat, resulting in a loss of efficiency and accelerated aging. To recuperate the portion of solar energy that is typically dissipated as heat while enhancing the efficiency of solar cells, a prototype hybrid PV/T (or PV-TE) collector has been designed and proposed [11,12].

Research has led to the identification of optimization strategies to increase the conversion efficiency of hybrid photovoltaic and thermoelectric systems. These systems have been perfected by incorporating a latent heat storage and cooling system and cooling fluids (air, water, nanofluids) into photovoltaic modules, resulting in a significant improvement in thermal performance and a consequent increase in the electrical energy produced by photovoltaic cells [12]. An air PV/T system is advantageous because it is easy to manage and can be directly used for heating purposes [13]. Free air convection cooling is a simple and cost-effective method for removing heat from the back of photovoltaic modules, thus maintaining an acceptable level of electrical efficiency [14]. Natural convection developing in this space helps dissipate the heat absorbed by the panels, thus reducing the temperature of the solar cells [15] and improving their electrical efficiency. Control of temperature for photovoltaic panels integrated into building structures has been researched by Brinkworth et al. [16]. Their study showed that transferring heat to an airflow behind the photovoltaic component can lead to temperature reductions of up to 20 K. As a result, there is a significant increase in electrical output and a decrease in heat gain within the building. Yang et al. [17] also performed research in this area and built a test setup consisting of a photovoltaic wall and roof to validate their simulation model. The design of a ventilated photovoltaic wall structure can reduce module temperatures by up to 15 °C and increase energy production by 8% compared to a non-ventilated structure. Nougblega et al. [18] investigated the thermal and electrical performance of hybrid collectors fitted with thermal screens. They found that the hybrid PV/T collector with an enclosed air gap has higher electrical efficiency. Many PV/T systems use air as the working fluid. However, incorporating an air gap behind the photovoltaic panels to limit heat transfer through the walls is less effective than anticipated [19,20]. Consequently, these air-based systems have become less attractive compared to other options. The presence of air within the pores or cells of the system precludes the transfer of heat by convection, due to the high viscous drag exerted on the cell walls. As a matter of fact, the utilization of alternative cooling channel structures is imperative to optimize the thermal and electrical performance of the PV/T system. A series of composite materials, superlattice materials, and low-dimensional carbon materials have become hot topics in recent years, such as SiGe, Bi_2Te_3, Sb_2Te_3, and graphene-based nanomaterials. Not much work has been conducted on adopting graphene to construct thermoelectric devices due to the lack of bulk fabrication and high thermal conductivity [12]. Many experimental works and theoretical models have been employed in investigating diverse performance development methods and design configurations of the hybrid PV/T system [21].

Senthilraja et al. [22] evaluated the performance of water-based and air-based PVT solar collectors. Their findings indicated a notable enhancement in thermoelectric performance for the water-based collector. Furthermore, PVT systems' performance can be enhanced by utilizing of innovative cooling channel structures, thereby optimizing the thermal and electrical performance of the PVT system. Some researchers have demonstrated the technical feasibility and performance characteristics of dual-fluid PVT (BFPVT) systems, which employ dual cooling exchangers and simultaneously deploy two distinct cooling fluids.

Abidi et al. [23] proposed combining a photovoltaic solar cell collector with an exchanger that has two fluids separated by a solid wall. The results show that this system can achieve enhanced operational performance if the nature and size of the fluid in contact with the photovoltaic cells and that of the solid wall are optimized. Aydin et al. [24] conducted an experimental and mathematical analysis of a novel cooling system utilizing Al_2O_3-water, TiO_2-water, and CuO-water nanofluids, incorporating thermal fins within the plate, to evaluate the thermoelectric efficiency of a PVT system in comparison with a water-cooled PVT panel. While all three nanofluids demonstrated notable cooling effects compared to water, the Al_2O_3-water nanofluid exhibited the most pronounced enhancement in electrical efficiency, with a temperature reduction of 13.28 °C, instead of 9.14 °C for water. Mohammed et al. [25] conducted a comparative study on the performance of a BFPVT system cooled simultaneously by natural air and a TiO_2-water nanofluid under two cooling channel configurations (with and without fins). The results show a considerable improvement for the finned configurations. Although these bi-fluid systems utilizing nanofluids demonstrate a notable enhancement, Irshad et al. [26] illustrated that the introduction of rare gases into a PVT collector could potentially achieve a higher level of efficiency than that achieved with air.

Based on the above discussions, it can be concluded that the PVT bi-fluid hybrid collector with fins offers promising prospects for improvement [25]. Nowadays, no studies have been reported in the literature regarding the energy performance of a PVT bi-fluid system incorporating a cooling fin and thermal screens of different enclosed gaps of noble gases, in particular neon, argon, and xenon, under the photovoltaic panel. The impact of this combination on the energy efficiency of photovoltaic (BIPV) panels integrated into buildings remains unexplored. However, this innovation could represent a significant opportunity for optimizing the thermoelectric performance of bi-fluid photovoltaic-thermal (BFPVT) systems. These are the several motivations of the authors to propose these innovative collectors in the present study.

We analyze the potential energy efficiency improvements associated with the use of heat shields filled with rare gases (neon, argon, xenon) compared with air in bi-fluid PVT systems incorporating copper fins. Pure copper is preferred for its high thermal conductivity and low energy losses at the storage outlet [27]. The performance evaluation includes the determination of electrical and thermal efficiency.

2. Mathematical formulation

2.1. Physical model

In the physical model shown in Figure 1a, a rectangular cavity of height H and width L is used, with a geometric aspect ratio of $A = H/L = 5$. The left vertical plate of the cavity on which the photovoltaic cells are integrated receives a constant flow of heat, while the right vertical plate is maintained at ambient temperature Ta; the horizontal walls are considered adiabatic. The cavity comprises two fluid compartments separated by the copper plate, which act as a solid cooling interface. The first cooling fluid, enclosed fluid 1, is in contact with the cells, while fluid 2 is in a ventilated channel with an inlet and an outlet. The model is assumed to be two-dimensional. Both fluids are assumed to be Newtonian and incompressible. Fluid 1 enclosed in the insulation cavity is characterized by thermal conductivity λ_{f1} and the convection coefficient h_{f1}, while fluid 2 is characterized by λ_{f2} and h_{f2}, Copper metal is defined by its specific conductivity λ_s and its thickness e_s. The flow is

considered to be stable and laminar. The thermophysical properties of the fluids are assumed to be constant except for the density, which is approximated in the gravity term with the Boussinesq approximation.

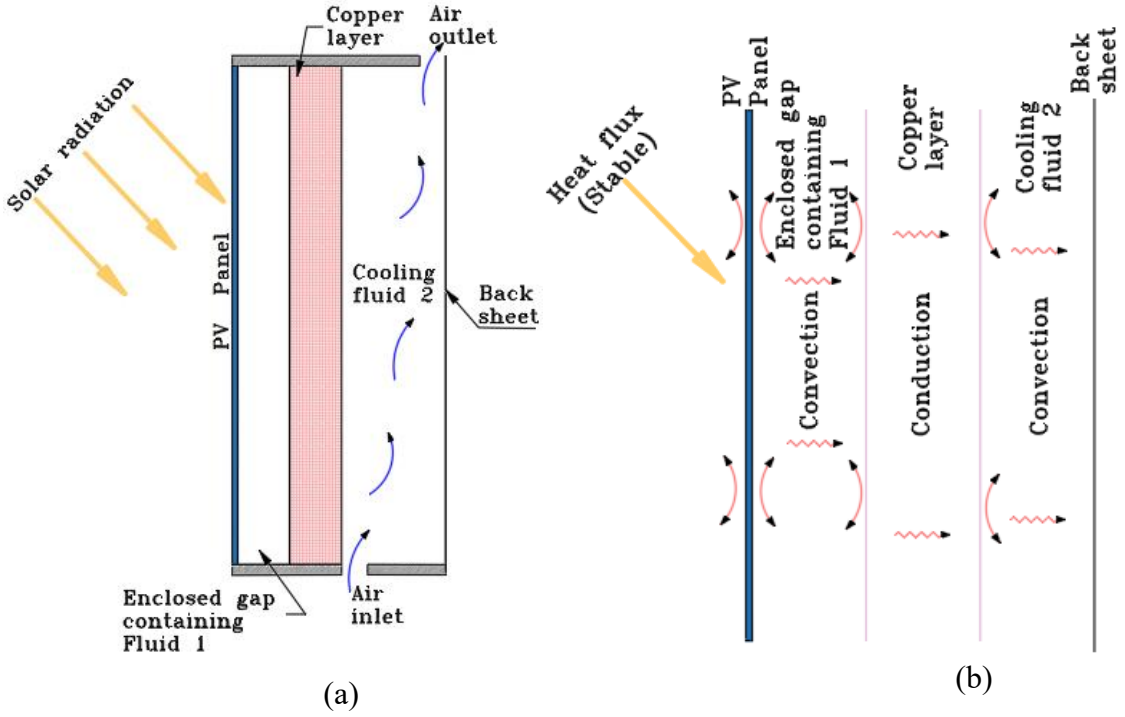

Figure 1. (a) Schematic diagram of the system (b) Flow chart for the heat transfer through the system.

In this study, radiation was excluded from consideration because its effect is insignificant for temperature variations below 100 °C [28]. Furthermore, the mean temperatures of photovoltaic cells equipped with heat exchangers, even under maximum irradiation of 1000 W/m², are typically below 40 °C [29]. This observation substantiates the exclusion of radiation from the analytical framework.

2.2. Dimensionless equations

2.2.1. Transfer equations

- On the level of the fluid

The non dimensional set of the governing equations (continuity, momentum, and energy equations) for a two-dimensional, incompressible laminar flow are the following:

$$\frac{\partial U}{\partial X} + \frac{\partial V}{\partial Y} = 0 \tag{1}$$

$$\frac{\partial \Omega}{\partial \tau} + U\frac{\partial \Omega}{\partial X} + V\frac{\partial \Omega}{\partial Y} = \frac{R_a}{P_r R_e^2}\frac{\partial \theta}{\partial X} + \frac{1}{Re}\left(\frac{\partial^2 \Omega}{\partial X^2} + \frac{\partial^2 \Omega}{\partial Y^2}\right) \tag{2}$$

$$\frac{\partial \theta}{\partial \tau} + U\frac{\partial \theta}{\partial X} + V\frac{\partial \theta}{\partial Y} = \frac{1}{R_e P_r}\left(\frac{\partial^2 \theta}{\partial X^2} + \frac{\partial^2 \theta}{\partial Y^2}\right) \tag{3}$$

$$\Omega = -\left(\frac{\partial^2\Psi}{\partial X^2}+\frac{\partial^2\Psi}{\partial Y^2}\right) \quad (4)$$

The stream function and vorticity are related to the velocity components by the following expressions:

$$U=\frac{\partial\Psi}{\partial Y}\ ; V=-\frac{\partial\Psi}{\partial X}\ ;\ \Omega=\frac{\partial V}{\partial X}-\frac{\partial U}{\partial Y} \quad (5)$$

- On the level of the solid

Conservation of energy equation:

$$\frac{\partial\theta}{\partial\tau}=\frac{a_r}{R_eP_r}\ \left(\frac{\partial^2\theta}{\partial X^2}+\frac{\partial^2\theta}{\partial Y^2}\right) where\ \ a_r=\frac{\lambda_r}{\rho_r Cp_r} \quad (6)$$

2.2.2. Initial and boundary conditions

- Initial conditions: at

$$\tau=0\ ,\theta=\Omega=\Psi=U=V=0 \quad (7)$$

- at $\tau > 0$, The boundary conditions associated with the problem are found below:

$$X=0\ and\ 0<Y<A; U=V=\ \Psi=0\ ;\ \Omega=-\frac{\partial^2\Psi}{\partial X^2}\Big|_{X=0}; -\frac{\partial\theta}{\partial X}\Big|_{X=0}=\tau_{pv}\alpha_{pv}-\eta_e \quad (8)$$

$$X=B_1\ and\ 0<Y<A; U=V=\Psi=0; \Omega=-\frac{\partial^2\Psi}{\partial X^2}\Big|_{X=B_1}\ ;\ -\frac{\partial\theta}{\partial X}\Big|_{X=B_1}=\tau_{pv}\alpha_{pv}\alpha_M-ABi_1\theta_S \quad (9)$$

$$X=B_2\ and\ 0<Y<A; U=V=\Psi=0; \Omega=-\frac{\partial^2\Psi}{\partial X^2}\Big|_{X=B_2}\ ; -\frac{\partial\theta}{\partial X}\Big|_{X=B_2}=\tau_{pv}\alpha_{pv}\alpha_M\tau_M+ABi_2\theta_S \quad (10)$$

$$X=1\ and\ 0<Y<A; U=V=\theta=\ 0; \Psi=-B_3+1,\ \Omega=\ -\ \frac{\partial^2\Psi}{\partial X^2}\Big|_{X=1} \quad (11)$$

$$Y=0\ and\ 0<X<B_1\ ; U=V=\Psi=0; \Omega=-\ \frac{\partial^2\Psi}{\partial Y^2}\Big|_{Y=0}\ ;\ \frac{\partial\theta}{\partial Y}\Big|_{Y=0}=0 \quad (12)$$

$$Y=0\ and\ B_2<X<B_3; U=\theta=0; V=1; \Psi=-X+1; \Omega=-\ \frac{\partial^2\Psi}{\partial Y^2}\Big|_{Y=0} \quad (13)$$

$$Y=0\ \ and\ B_3<X<1; U=V=0\ ; \Psi=-B_3+1;\ \Omega=-\ \frac{\partial^2\Psi}{\partial Y^2}\Big|_{Y=0}\ ;\ \frac{\partial\theta}{\partial Y}\Big|_{Y=0}=0 \quad (14)$$

$$Y=A\ \ and\ 0<X<B_4;\ U=V=\Psi=0\ ;\ \Omega=\ -\ \frac{\partial^2\Psi}{\partial Y^2}\Big|_{Y=A}\ ;\ \frac{\partial\theta}{\partial Y}\Big|_{Y=A}=0 \quad (15)$$

$$Y=A\ and\ \ B_4<X<1\ ;\ U=0\ ;\frac{\partial V}{\partial Y}\Big|_{Y=A}=\ \frac{\partial\Psi}{\partial Y}\Big|_{Y=A}=\frac{\partial\Omega}{\partial Y}\Big|_{Y=A}=\frac{\partial\theta}{\partial Y}\Big|_{Y=A}=0 \quad (16)$$

The fluid 1 convection coefficient is estimated by Woodfield et al. [30]:

$$h_{f1} = \frac{q}{|T_{f1} - T_{copper}|} \tag{17}$$

The fluid 2 convection coefficient is estimated from the wind velocity by palyvos [31]:

$$h_{f2} = 5.62 + 3.9V_{wind} \tag{18}$$

2.3. Evaluation of heat transfer intensity

Heat transfer through photovoltaic modules is best represented by the Nusselt number, which is a measure of the ratio of conductive heat transfer to convective flow through the cooling fluid. The local Nusselt number on the inner plate of PV cells is given by:

$$N_{uPV} = 1/\theta_{PV}. \tag{19}$$

The electrical and thermal efficiencies of the photovoltaic-thermal hybrid collector are as follows respectively:

$$\eta_{el} = \eta_{ref} - \beta_{PV}\left(\overline{T_{PV}} - T_{ref}\right) \ With \ \overline{T_{PV}} = \frac{1}{H}\int_0^H T_{PV}(y)dy \tag{20}$$

$$\eta_{th} = D_m C_p (T_{out} - T_{int})/(\phi H) \tag{21}$$

The mass flow rate in the channel is expressed:

$$D_m = (\rho V_0/(1 - B_2)\int_{B_2}^1 V(X, A)dX \tag{22}$$

$\overline{T_{PV}}$ is the average absolute temperature of the PV plate, T_{out}, T_{int} are respectively the outlet and the inlet absolute temperature of the air in the ventilated canal.

3. Numerical procedure

To discretize the non-linear partial differential Eqs (1–3), we used an implicit finite difference method. We approximated the first and second derivatives of the diffusive terms using centered finite differences, and the convective terms were approximated using a second-order scheme to avoid the potential instabilities often encountered in mixed convection flow problems. The system of differential equations was transformed into a linear algebraic system, which we solved using the Thomas algorithm. At each time step, we solved the Poisson Eq (4) using the successive point sub-relaxation (PSUR) method with an optimal sub-relaxation coefficient of 0.8 for the (201 × 41) grid used in our study. This approach's advantage lies in using the Gauss-Seidel method to obtain an intermediate iterate, denoted as ϕ^{k+1}, which is then "relaxed" to accelerate convergence. Furthermore, the Gauss-Seidel method is straightforward to program. We achieved convergence of the iteration for the stream function solution at each time step, and employed a criterion to check for a steady-state solution. Convergence of solutions is assumed when the relative error for each variable between consecutive iterations is below the convergence criterion ε such that $\sum|(\phi_{i,j}^{k+1} - \phi_{i,j}^{k})/\phi_{i,j}^{k+1}| < 10^{-5}$, where ϕ stands for ψ, Θ, ω, k refers to time and i and j refer to space coordinates. The time step used in the computations is $\Delta\tau = 10^{-5}$. To reduce the influence of the mesh on simulation accuracy, mesh independency solutions are assured by comparing different grid meshes for the highest Rayleigh and Reynolds numbers used

in this work (Ra = 10^6 and Re = 50). The non-uniform 101 × 21 and 201 × 41 meshes result in minor discrepancies in the characteristic quantities Ψ, Θ, and *Nu* compared to the uniform 101 × 101 and 201 × 201 meshes, as illustrated in Table 1. Adopting a non-uniform mesh optimizes resolution, providing a superior geometric representation of the model while reducing numerical errors and improving computational efficiency. However, the 201 × 41 mesh was selected due to its enhanced efficiency in heat transfer compared to the 101 × 21 mesh, as evidenced by a 0.04641% increase in the Nusselt number. The solution flowchart, which provides an overview of the methodology employed in the resolution of the numerical schemes associated with the problem, is presented in Figure 2.

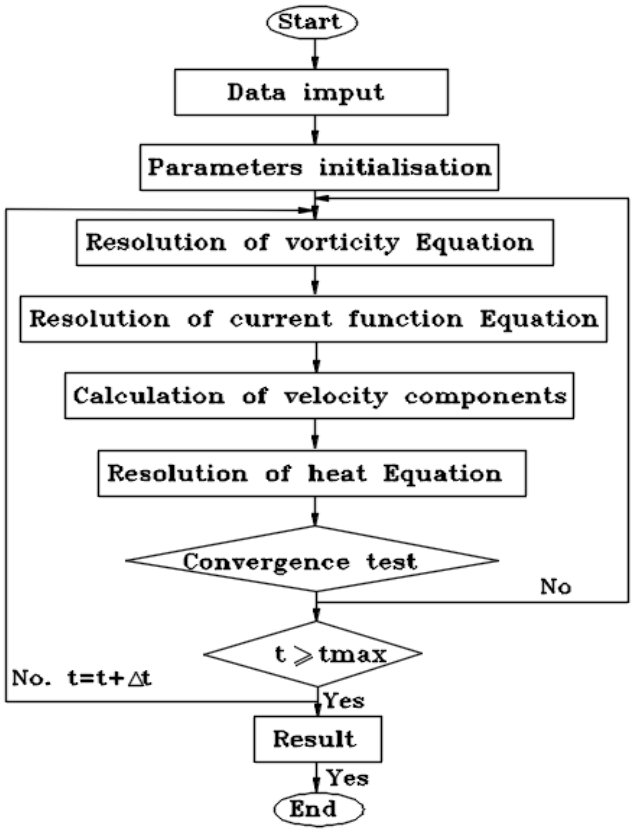

Figure 2. Flow chart for the resolution of the system of algebraic transfer equations.

Table 1. Grid Independency.

Stage	Ψmax	Change (%)	Θmax	Change (%)	Numax	Change (%)
101X21	9.507E-06	˜	5.725E-02	˜	1.747E+01	˜
201X41	8.056E-06	1.451E-04	5.372E-02	3.526E-01	1.751E+01	4.641E-02
101X101	9.315E-06	˜	1.780E-02	˜	5.617E+01	˜
201X201	6.693E-06	2.621E-04	8.903E-03	8.901E-01	5.672E+01	5.533E-01

The vorticity computational formula of Woods [32] for approximating the wall vorticity was used: $\Omega(P) = \frac{1}{2}\Omega_{P+1} - \frac{3}{\Delta\eta^2}(\psi_{P+1} - \psi_P)$, where ψ_P and ψ_{P+1} are stream function values at the points adjacent to the boundary wall; η, the normal abscise on the boundary wall.

4. Results and discussion

4.1. Validation

The numerical code has been validated by literature data against the work results by Han et al. [33]. Han et al. studied heat transfer by natural convection in a closed-air cavity to evaluate the thermal performance of the cavity of the glazing system integrated with PV cells. Comparisons made in terms of streamlines and isotherms for Raleigh number, Ra = 5.10^4, a uniform grid 36 × 36 with Pr = 0.71 and Re = 1 (pure natural convection) showed fairly good agreement (Figure 3).

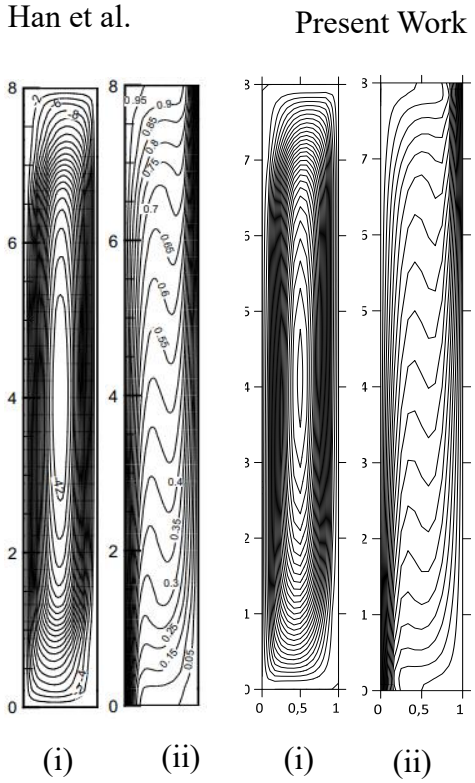

Figure 3. Comparison of Streamlines (i) and isotherms (ii).

Table 2 presents a quantitative validation of the electrical efficiency model (Eq 20). According to this model, a 1 °C increase in the average temperature of PV cells results in a 0.067% reduction in electrical efficiency. This finding is corroborated by the findings of Rahman et al. [34], who indicated that at an irradiance of 1000 W/m², the electrical efficiency decreases by 0.06% for each 1 °C increase in solar cell temperature.

Table 2. Comparison of the impact of temperature on PV cell efficiency in the current modeling approach with that of Rahman et al. [34].

	$\mathbf{T_{PVmoy}}$(K)	Change (°C)	$\boldsymbol{\eta_{elmoy}}$(%)	Change(%)
Present work	298	-	15	-
	308	10	14.3250006	−0.6749994
Rahman et al.	-	1	-	0.06

Table 3. Numerical model input parameters.

Parameters	Value
Absorptivity of PV cells surface, $\boldsymbol{\alpha_{pv}}$	0.89 (-)
Transmittance of PV cells surface, $\boldsymbol{\tau_{pv}}$	0.09 (-)
Absorptivity of the copper surface, $\boldsymbol{\alpha_{Cu}}$	0.38
Transmittance of the copper surface, $\boldsymbol{\tau_{Cu}}$	0.678
Reference temperature, $\boldsymbol{T_{ref}}$	298 K
Electrical efficiency at the reference temperature, $\boldsymbol{\eta_{ref}}$	0.015 (-)
Temperature coefficient of PV cell, $\boldsymbol{\beta_{ref}}$	0.0045 K^{-1}

4.2. Effect of the fluid-enclosed gap on the thermoelectric performance of the collector

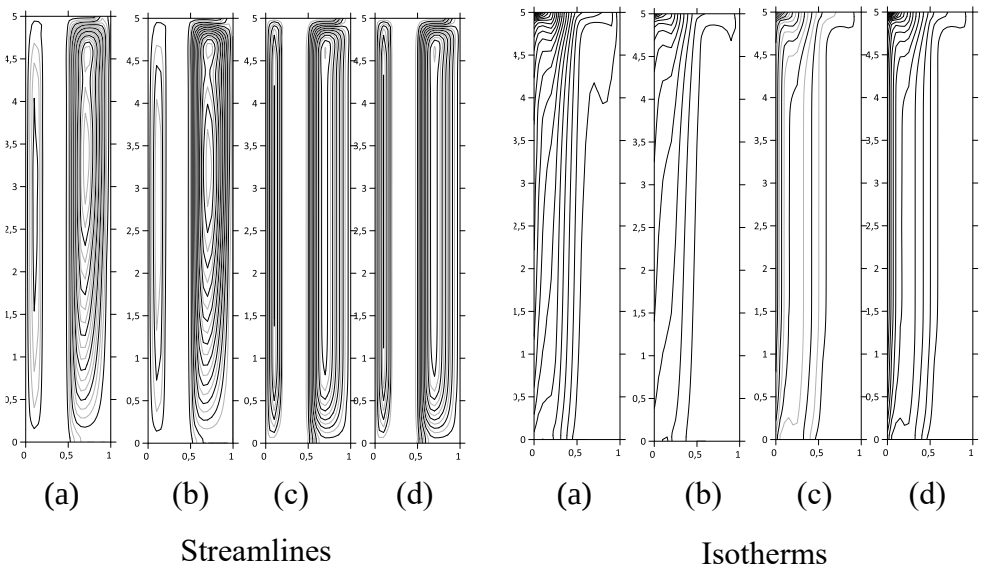

Figure 4. Streamlines and isotherms obtained for Bi_1 et Bi_2 < 0.1, Ra = 5.10^6, Re = 50 for the thermal screen of the enclosed gap of different fluids (a) Air ;(b) Neon; (c) Argon; (d) Xenon.

Figure 4 illustrates the influence of the thermal screen of the enclosed gap of different fluids on the flow and the thermal distribution. The confined channel, situated between the photovoltaic cells and the solid cooling interface, is predominantly influenced by natural convection, manifested as backflow Han et al. [33]. In contrast, the open channel facilitates the removal of excess heat through forced convection. In the confined channel, natural convection is based on the principle of buoyancy, whereby the flow of air, resulting from variations in density, ensures stable thermal circulation and optimizes heat transfer from the photovoltaic cells to the copper, as demonstrated by Akshayveer et al. [35]. Conversely, forced convection, as indicated by the presence of open lines resulting from the influx of fresh air into the open channel, accelerates the removal of heat, thereby preventing overheating and enhancing the overall thermal efficiency of the system, as demonstrated by Alibakhsh et al. [36]. Saber Boulhidja et al. [37] highlight that the coexistence of natural convection and forced convection (mixed convection), reflected by the coexistence of open and closed lines, enhances heat transfer, stabilizing thermal and electrical performance by maintaining the photovoltaic cells at an optimal operating temperature. This is exemplified by Argon and Xenon collectors, where

the intensity of heat exchange is at its maximum, as illustrated in Figure 5a. In air and neon collectors where natural convection is the dominant mechanism, the system cannot effectively remove excess heat, resulting in overheating of the photovoltaic cells and a subsequent reduction in their electrical efficiency. This phenomenon is illustrated in Figures 8a and 9a. The isotherms in the solid (copper) are very tight and almost parallel; indicating that heat transfer is mainly by conduction. In the fluid enclosures of the collector, the isotherms bifurcate, indicating the existence of heat transfer by convection.

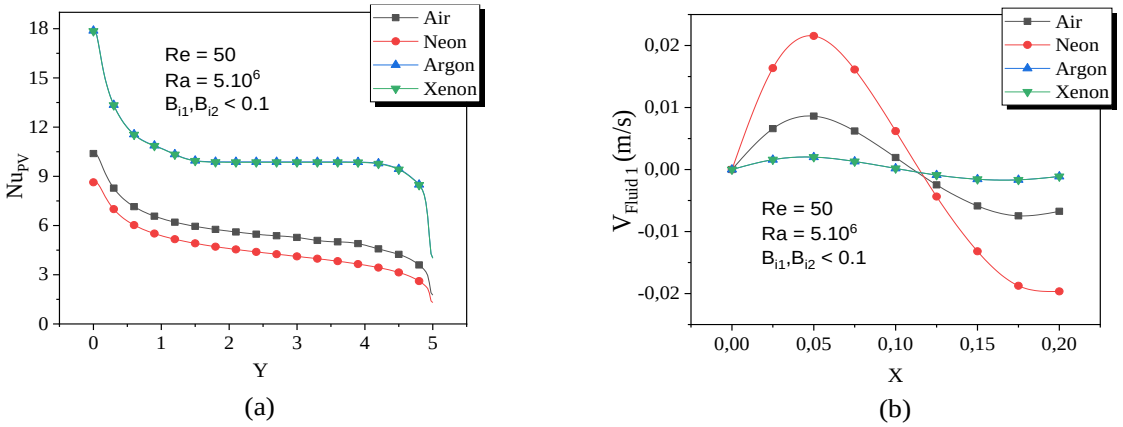

Figure 5. (a) Local Nusselt number along the PV cells and (b) Vertical velocity at mid-height for the thermal screen of the enclosed gap of different fluids.

The variation of the local Nusselt number with the Y coordinate along the PV cell plate is shown in Figure 5a. In general, the Nusselt number at the PV cell plate begins with a high value at a point near the bottom and decreases monotonically to a small value at the top; similar results have been obtained by Nougblega et al. [38] and Han et al. [33]. Figure 5b illustrates the vertical velocity profiles at half-height for the different fluids. In the first half of the fluid 1 enclosure, the velocity of fluid 1 increases successively from Xenon, argon, and air to Neon, whose velocity at half-height is greater. In contrast, it is a decreasing function in the same direction for the fluids in the second half. The appearance of the half-height vertical velocity curves obtained is comparable to the results of Abidi et al. [23], this means that the flow of fluid 1 is dominated by natural convection.

The variation of the local Nusselt number along the photovoltaic cells is higher in the cases of argon and xenon compared to air. Conversely, a decrease is observed for neon, with a negative variation, as illustrated in Figure 6. The Nusselt number is a quantitative measure of the relative contribution of heat transfer by convection compared with conduction in a given flow situation. A high Nusselt number reflects a significant improvement in heat transfer due to fluid motion, which optimizes the thermal and electrical performance of the system. This is demonstrated by Nahar et al. [39]. For example, argon and xenon provide optimized thermal management by convection compared with air, maintaining photovoltaic cells at an ideal temperature and, therefore, improving their electrical efficiency. This is illustrated in Figures 8a and 9a.

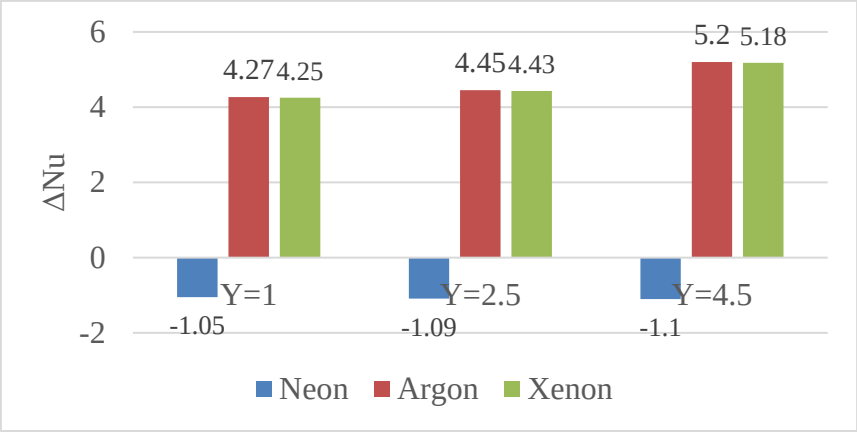

Figure 6. Variation of the local Nusselt number along the PV cells for neon, argon, and xenon for air ΔN_u at positions Y = 1; 2.5 and 4.5.

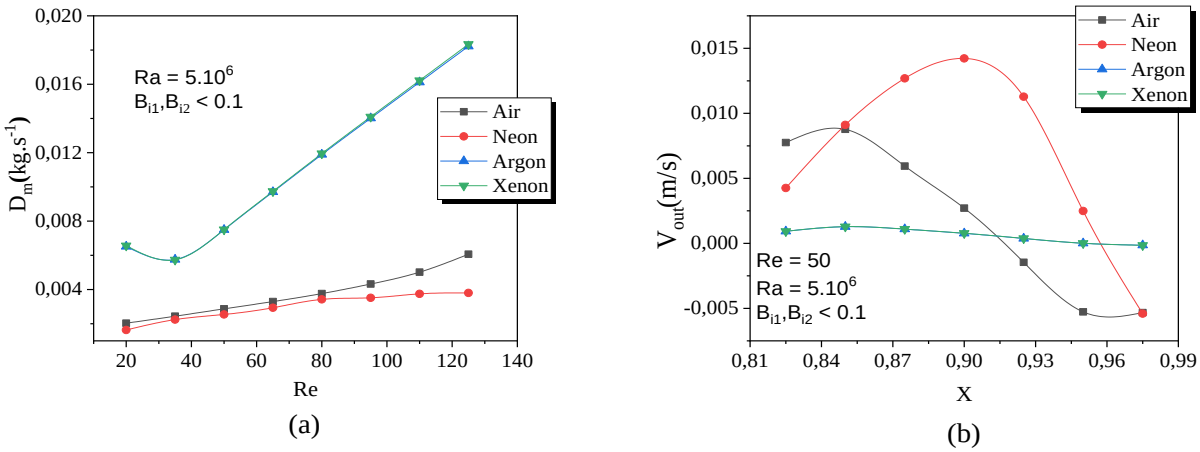

Figure 7. (a) Variation of air mass flow rate versus Reynolds and (b) Variation of air outlet velocity for the thermal screen of the enclosed gap of different fluids.

The velocity of the outlet airflow increases and reaches a maximum value in the middle of the fluid flow duct 2 before decreasing to reach the minimum value near the rear wall set at ambient temperature, as shown in Figure 7b. This situation means that the air molecules close to the insulated wall, which do not have the energy to leave the channel, return to their exit trajectory, and, as a result, advection occurs, which explains the negative values of the velocity. The positive values of the ascending velocity in the first half of the lower channel of the bi-fluid collector show the existence of the thermosiphon phenomenon of the heat transfer air in this duct. These phenomena were intense for the Argon and Xenon collectors and less intense for the Air and Neon collectors, as shown in Figure 7a. The Argon and Xenon collectors considerably improve the air draft in the ventilated cavity.

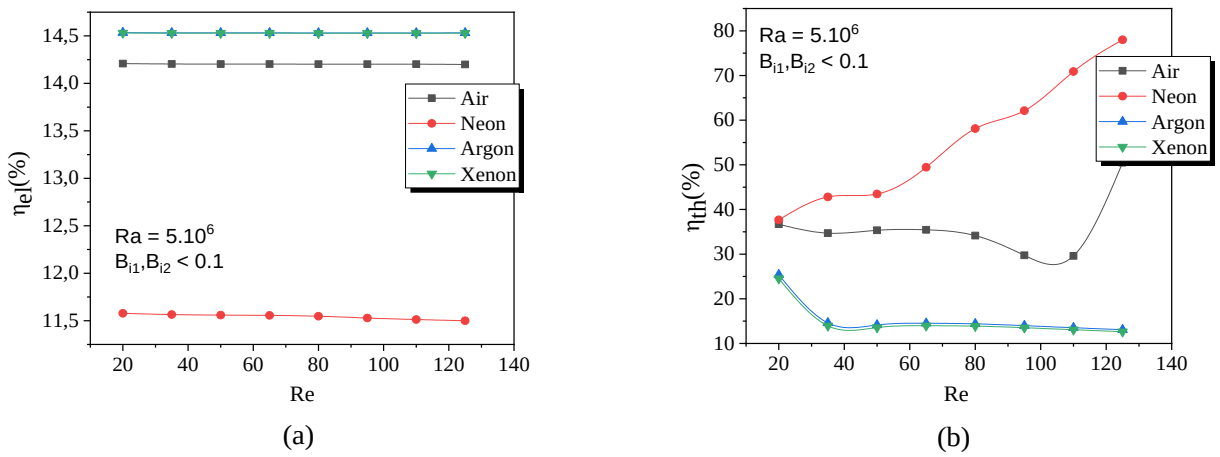

Figure 8. (a) Variation of electrical efficiency versus Reynolds number and (b) Variation of thermal efficiency versus Reynolds number for the thermal screen of the enclosed gap of different fluids.

As shown in Figures 8a and 9a, the electrical efficiency of photovoltaic solar cells is a decreasing function of both Reynolds and Rayleigh numbers. Xenon and Argon collectors show the best electrical efficiencies compared with Air and Neon collectors; however, the latter two show the best thermal efficiencies (Figures 8b and 9b). Table 4 shows the thermoelectric performance of PVT bi-fluid collectors fitted with heat shields of enclosed gaps of different fluids. The electrical efficiency and cooling capacity of argon- and xenon-filled collectors are noteworthy attributes. However, while xenon exhibits an excellent coefficient of performance, its global warming potential (GWP) is higher than that of argon although xenon is not a direct greenhouse gas, as highlighted by Tobechi et al. [40]. The economic viability of xenon is limited. Conversely, argon is the optimal filling gas, considering both economic and environmental criteria.

Table 4. Comparison of the thermoelectric performance of PVT collectors operating with neon, argon, and xenon, compared with an air collector for a reference electrical efficiency η_ref = 15% and an initial temperature Ta = 298 K.

Fluid 1	$\mathbf{T_{PVmoy}}$(K)	Change (°C)	$\boldsymbol{\eta_{thmoy}}$(%)	Change (%)	$\boldsymbol{\eta_{elmoy}}$(%)	Change (%)
Air	309,95	-	33,67	-	14,20	-
Neon	349,27	39.32	52,073	18.40	11,55	−2.65
Argon	305,08	−4.87	15,46	−18.21	14,53	0.33
Xenon	305,13	−4.82	14,89	−18.78	14,53	0.33

The notable disparity in thermal efficiency between argon (15.46%) and neon (52.07%) is attributable to several pivotal physical attributes of neon. Neon exhibits superior thermal conductivity, which enhances heat transfer, and a lower heat capacity, enabling more efficient absorption and dissipation of heat, as evidenced by Tang et al. [41]. Furthermore, its lower density facilitates enhanced thermal circulation, contributing to an elevated level of thermal performance [42].

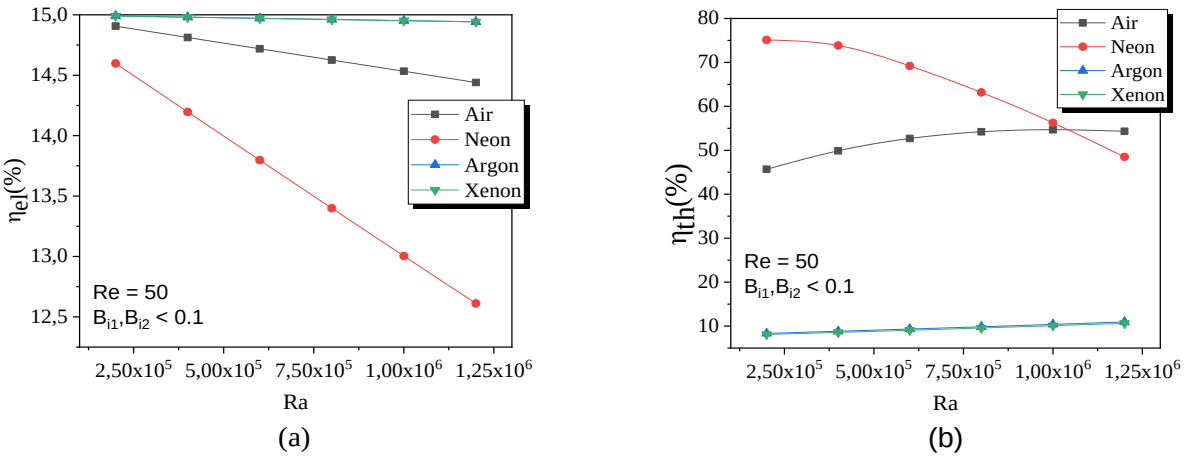

Figure 9. (a) Variation of electrical efficiency versus Rayleigh number and (b) Variation of thermal efficiency versus Rayleigh number for the thermal screen of the enclosed gap of different fluids.

4.3. Effects of Reynolds and Rayleigh numbers on the thermoelectric performance of the Argon collector

4.3.1. Effect of Reynolds number

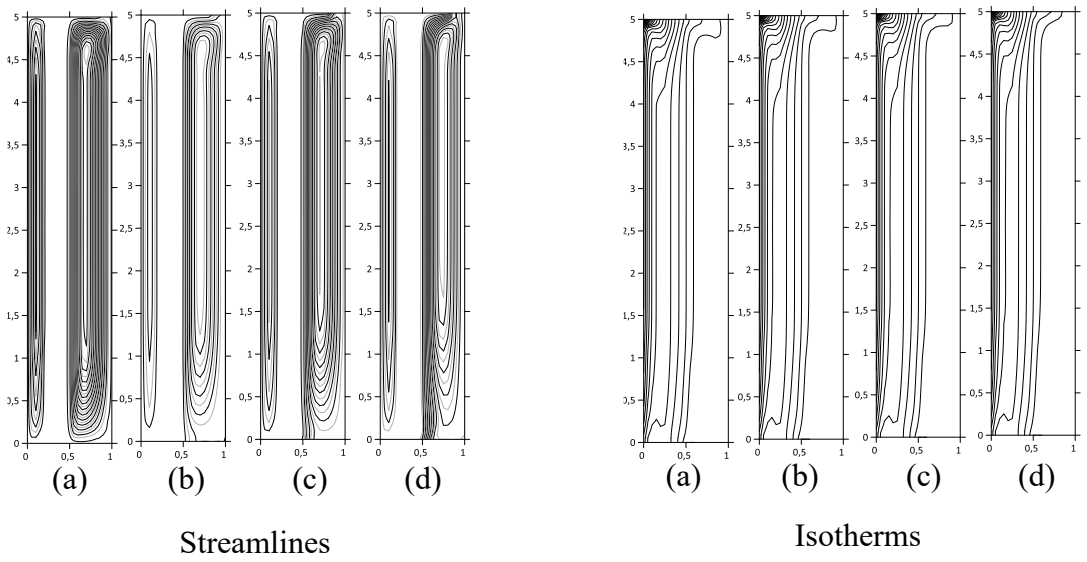

Figure 10. Streamlines and isotherms for Ra = 5.10^6 and for various Re: (a) Re = 25; (b) Re = 50; (c) Re = 75; (d) Re = 100.

The streamlines and isotherms for different Reynolds number values with a Rayleigh number fixed at Ra = 5.10^6 and Biot numbers Bi_1 and Bi_2 < 0.1 are shown in Figure 10. It can be noted that for low Reynolds number values, closed cells of natural convection are present and abundant. When natural convection is the dominant mechanism in a closed argon-filled cavity, high Reynolds number values can result in a reduction in the efficiency of the system. At low Reynolds number values (Re),

natural convection is efficient, and heat transfer is optimal, as illustrated in Figure 11. However, an excessive increase in Re, which introduces turbulent regimes, can disrupt the natural convection cells, leading to a loss of efficiency. Betts et al. [43] demonstrated that elevated Re disrupts natural convection regimes, resulting in a reduction in the heat transfer rate and Nusselt number. At exceedingly high Re, thermoelectric efficiency may decline due to the disruption of natural convection. Consequently, the electrical efficiency of the collector declines with increasing Re, as illustrated in Figure 12.

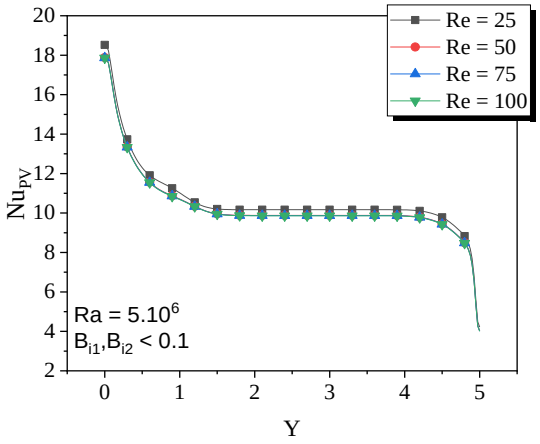

Figure 11. Local Nusselt number along the PV cells.

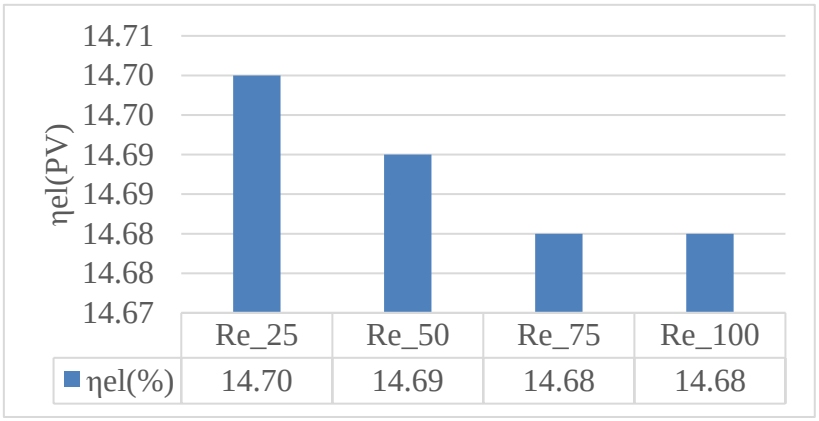

Figure 12. Electrical performance of the Argon PV/T collector for different Re and Ra = 5.10^6.

4.3.2. Effect of Rayleigh number

Figure 13 shows the variation of streamlines and isotherms for different values of Rayleigh number with a fixed Reynolds number (Re = 50) and Biot numbers; Bi_1 and Bi_2 < 0.1. The flow structure varies with increasing Rayleigh number. For low Rayleigh numbers, authors note the coexistence of open and closed lines; this situation shows that for low values of the Rayleigh number, mixed convection takes hold in the open channel; however, the closed lines decrease in the closed cavity containing fluid 1.

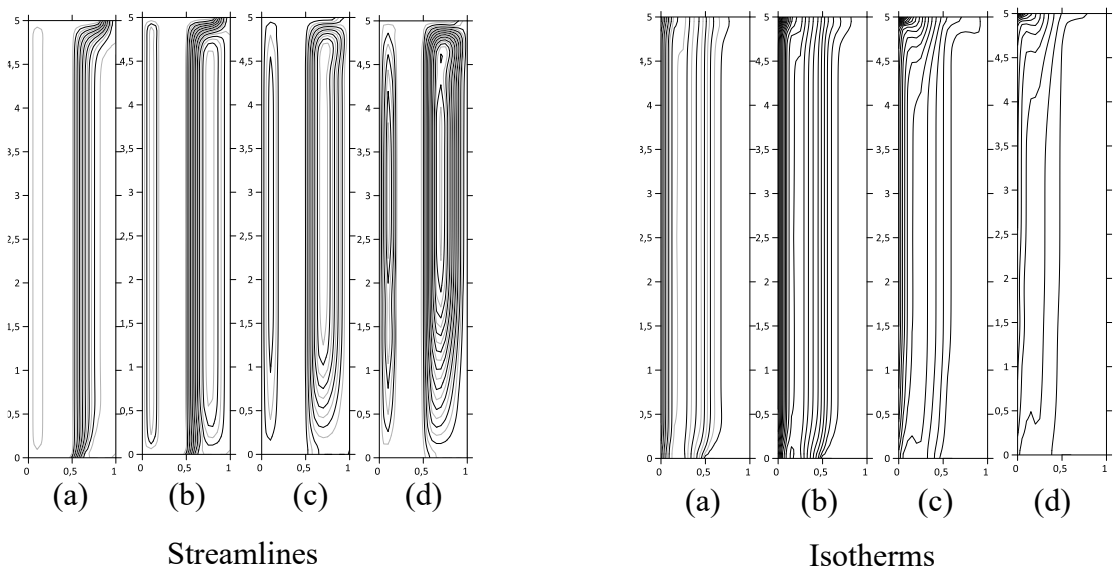

Figure 13. Streamlines and isotherms for Re = 50 and different Ra: (a) Ra = 5.10^5; (b) Ra = 1.10^6; (c) Ra = 5.10^6; (d) Ra = 1.10^7.

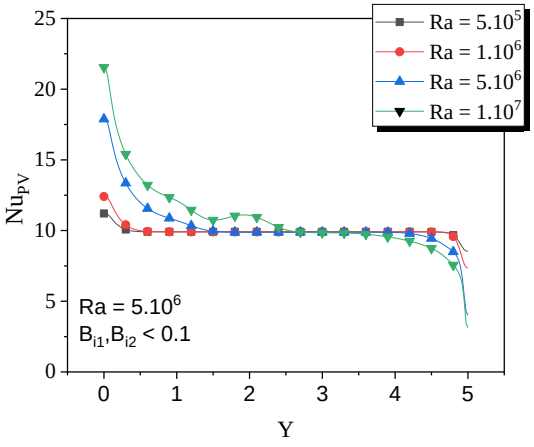

Figure 14. Local Nusselt number along the PV cells.

The isotherm pattern shows that the dominant transfer mode is conduction at low Rayleigh numbers. As the Rayleigh number increases, the size of the counter-rotating cells increases, indicating an increase in natural convection. In the case of exceedingly high values of the Rayleigh number, there is a potential for a reduction in heat transfer efficiency. Although a high Rayleigh number (Ra) indicates strong natural convection, an excessive Ra can lead to instabilities and saturation of convective effects. Batchelor et al. [44] observed that very high Rayleigh numbers lead to instabilities that limit heat transfer efficiency and can even reduce the Nusselt number. This finding is confirmed in Figure 14. Consequently, the electrical efficiency of the sensor decreases with the Rayleigh number, as shown in Figure 15.

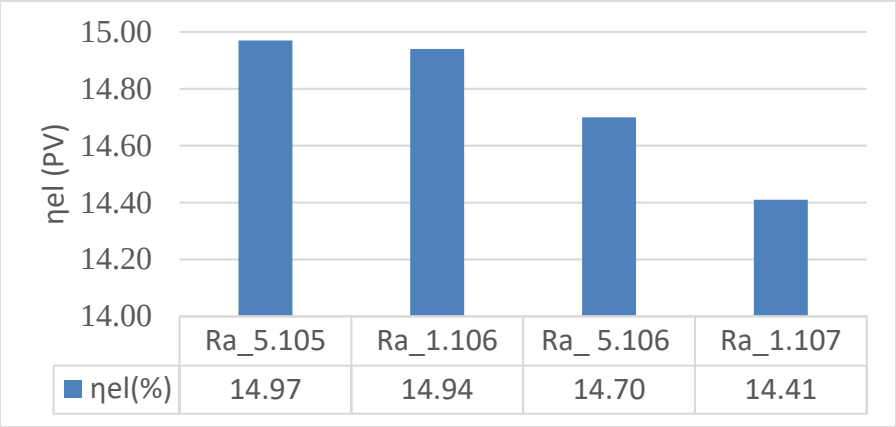

Figure 15. Electrical performance of the Argon PVT collector for different Ra and Re = 50.

5. Conclusions

To optimize the performance of a building-integrated photovoltaic/thermal hybrid system, a numerical model was developed for a collector of photovoltaic cells combined with a dual-fluid heat exchanger, where the two fluids are in contact with a copper interface. The heat exchanger is equipped with a fluid-filled heat shield. An analysis was conducted to evaluate the influence of the fluids present in the heat shield, including neon, argon, and xenon, in comparison with air, on the thermal and electrical performance of the collector. Furthermore, the impact of control parameters, particularly Reynolds and Rayleigh numbers, on heat transfer was investigated to anticipate the thermoelectric behavior of the PVT collector. For Biot numbers $Bi_1, Bi_2 < 0.1$, where the temperature can be regarded as uniform in the thin solid, we identified the following key findings from the analyses:

- When air was replaced by xenon and argon as the filler gases for the heat shield, the average temperature of the photovoltaic cells significantly decreased by 4.82 °C and 4.87 °C, respectively.
- Electrical performance of the photovoltaic cells insulated with argon and xenon-enclosed gap demonstrated an improvement of 0.33% compared to that of the cells in the air-filled photovoltaic-thermal collector.
- Given the scarcity and high cost of xenon compared to argon, it is recommended that argon be used as the insulating fluid for solar cells in dual-fluid photovoltaic-thermal collectors.
- Thermal efficiency of the solar cells exhibited an 18% enhancement in the dual-fluid neon photovoltaic-thermal collector relative to the air photovoltaic-thermal collector.
- High Reynolds number values disrupt natural convection regimes, reducing the heat transfer rate and, consequently, a decrease in the electrical efficiency of photovoltaic cells.
- Electrical efficiency decreases with high Rayleigh numbers due to disruption of the convection regimes developed in the channels of the two-fluid collector.

From this perspective, we are engaged in further research, including the utilization of disparate nanofluids in conjunction with cooling materials as heat transfer fluids, to enhance the performance of the PV/T dual-fluid collector.

Use of AI tools declaration

The authors declare they have not used Artificial Intelligence (AI) tools in the creation of this article.

Acknowledgments

This work was supported by the Regional Centre of Excellence on Electricity Management (CERME) at the University of Lomé. With these words, the authors express their gratitude to the CERME.

Funding

This work has been supported by the Regional Center of Excellence for Electricity Management (CERME).

Conflict of interest

The authors declare no conflicts of interest.

Author contributions

K.A.T. worked research for the paper, while K.A.A. contributed to the writing and provided the necessary methodology. Y.N. supervised the project. All authors have read and approved the final version of the manuscript.

References

1. Roques P, Roux D (2018) Consommation d'énergie et théorie des pratiques: vers des pistes d'action pour la transition énergétique. *Décisions Mark* 90: 35–54. https://doi.org/10.7193/dm.090.35.54
2. Parida B, Iniyan S, Goic R (2011) A review of solar photovoltaic technologies. *Renewable Sustainable Energy Rev* 15: 1625–1636. https://doi.org/10.1016/j.rser.2010.11.032
3. Maghrabie H, Elsaid K, Sayed E, et al. (2021) Building-integrated photovoltaic/thermal (BIPVT) systems: Applications and challenges. *Sustainable Energy Technol Assess* 45. https://doi.org/10.1016/j.seta.2021.101151
4. Marei Y, Emam M, Ahmed M, et al. (2024) Thermal and optical investigations of various transparent wall configurations and building integrated photovoltaic for energy savings in buildings. *Energy Convers Manage*, 299. https://doi.org/10.1016/j.enconman.2023.117817
5. Mohamed E, Moustafa M, Chazy M (2023) Design of solar air conditioning system integrated with photovoltaic panels and thermoelectric coolers: Experimental analysis and machine learning modeling by random vector functional link coupled with white whale optimization. *Therm Sci Eng Prog* 43: 102051. https://doi.org/10.1016/j.tsep.2023.102051

6. Şirin C, Goggins J, Hajdukiewicz M (2023) A review on building-integrated photovoltaic/thermal systems for green buildings. *Appl Therm Eng*, 229. https://doi.org/10.1016/j.applthermaleng.2023.120607
7. Krauter S, Araújo RG, Schroer S, et al. (1999) Combined photovoltaic and solar thermal systems for facade integration and building insulation. *Sol Energy* 67: 239–248. https://doi.org/10.1016/S0038-092X(00)00071-2
8. Antonanzas J, Del Amo A, Martinez-Gracia A, et al. (2015) Towards the optimization of convective losses in photovoltaic-thermal panels. *Sol Energy* 116: 323–336. https://doi.org/10.1016/j.solener.2015.04.013
9. Ben C, Marir-Benabbas M (2023) Etude des performances électriques et thermiques d'un capteur hybride PVT. *J Renewable Energy* 16: 257–268. https://doi.org/10.54966/jreen.v16i2.378
10. Kant K, Shukla A, Sharma A, et al. (2016) Thermal response of poly-crystalline silicon photovoltaic panels: Numerical simulation and experimental study. *Sol Energy* 134: 147–155. https://doi.org/10.1016/j.solener.2016.05.002
11. Wolf M (1976) Performance analyses of combined heating and photovoltaic power systems for residences. *Energy Convers* 16: 79–90. https://doi.org/10.1016/0013-7480(76)90018-8
12. Jian T, Hao N, Run-Ling P, et al. (2023) A review on energy conversion using hybrid photovoltaic and thermoelectric systems. *J Power Sources*, 562. https://doi.org/10.1016/j.jpowsour.2023.232785
13. Yu J, Kim J, Kim J (2020) Effect of triangular baffle arrangement on heat transfer enhancement of air-type PVT collector. *Sustainability (Switzerland)*, 12. https://doi.org/10.3390/SU12187469
14. Chow T, Hand J, Strachan P (2003) Building-integrated photovoltaic and thermal applications in a subtropical hotel building. *Appl Therm Eng* 23: 2035–2049. https://doi.org/10.1016/S1359-4311(03)00183-2
15. Wei D, Qirong Y, Jincui Z (2011) A study of the ventilation performance of a series of connected solar chimneys integrated with building. *Renewable Energy* 36: 265–271. https://doi.org/10.1016/j.renene.2010.06.030
16. Brinkworth B, Cross B, Marshall R, et al. (1997) Thermal regulation of photovoltaic cladding. *Sol Energy* 61: 169–178. https://doi.org/10.1016/S0038-092X (97)00044-3
17. Yang H, Marshall R, Brinkworth B (1996) Validated simulation for thermal regulation of photovoltaic wall structures. *Conference Record of the IEEE Photovoltaic Specialists Conference* 3: 1453–1456. https://doi.org/10.1109/pvsc.1996.564409
18. Nougbléga Y, Kpode K, Atchonouglo K, et al. (2018) Effect of enclosed air gap and empty gap for thermal screens in PV cells isolation inside the hybrid photovoltaic-thermal channel on a rooftop designed for natural ventilation in bioclimatic buildings. *Int J Sci Technol Res* 7: 112–121.
19. Yu G, Yang H, Yan Z, et al. (2021) A review of designs and performance of façade-based building integrated photovoltaic-thermal (BIPVT) systems. *Appl Therm Eng*, 182. https://doi.org/10.1016/j.applthermaleng.2020.116081
20. Aspetakis G, Wang Q (2025) Critical review of Air-Based PVT technology and its integration to building energy systems. *Energy Built Environ* 6: 121–135. https://doi.org/10.1016/j.enbenv.2023.10.001
21. Elnozahy A, Rahman AKA, Ali AHH, et al. (2015) Performance of a PV module integrated with standalone building in hot arid areas as enhanced by surface cooling and cleaning. *Energy Build* 88: 100–109. https://doi.org/10.1016/j.enbuild.2014.12.012

22. Senthilraja S, Gangadevi R, Marimuthu R, et al. (2020) Performance evaluation of water and air based PVT solar collector for hydrogen production application. *Int J Hydrogen Energy* 45: 7498–7507. https://doi.org/ 10.1016/j.ijhydene.2019.02.223
23. Abidi S, Sammouda H, Bennacer R (2014) Numerical analysis of three coolants heat exchanger associated to hybrid photovoltaic thermal solar sensor. *Int J Energy Eng* 4: 45–53. https://doi.org/10.5923/j.ijee.20140403.01
24. Aydın A, İsmail K, Hüseyin A (2024) Electrical and thermal performance enhancement of a photovoltaic thermal hybrid system with a novel inner plate-finned collective cooling with different nanofluids. *Int J Green Energy*, 21. https://doi.org/10.1080/15435075.2023.2201345
25. Mohammed E, Mohamed EZ, Kabeel AE, et al. (2024) Numerical analysis and design of a novel solar photovoltaic thermal system using finned cooling channel structures embedded with air/TiO_2—water nano bi-fluid. *Sol Energy*, 269. https://doi.org/10.1016/j.solener.2024.112368
26. Irshad K, Habib K, Thirumalaiswamy N (2015) Performance evaluation of PV-Trombe wall for sustainable building development. *Procedia CIRP* 26: 624–629. https://doi.org/10.1016/j.procir.2014.07.116
27. Calderón-Vásquez I, Segovia V, Cardemil JM, et al. (2021) Assessing the use of copper slags as thermal energy storage material for packed-bed systems. *Energy*, 227. https://doi.org/10.1016/j.energy.2021.120370
28. Luc L (2014) Law of cooling, heat conduction and Stefan-Boltzmann radiation laws fitted to experimental data for bones irradiated by CO_2 laser. *Biomed Opt Express* 5: 701–712. https://doi.org/10.1364/BOE.5.000701
29. Mohamed G, Mohsen A, Hegazy R (2022) Temperature distribution modeling of PV and cooling water PV/T collectors through thin and thick cooling cross-fined channel box. *Energy Rep* 8: 1144–1153. https://doi.org/10.1016/j.egyr.2021.11.061
30. Woodfield P, Monde M, Mitsutake Y (2007) Measurement of averaged heat transfer coefficients in high-pressure vessel during charging with hydrogen, nitrogen or argon gas. *J Therm Sci Technol* 2: 180–191. https://doi.org/10.1299/jtst.2.180
31. Palyvos J (2008) A survey of wind convection coefficient correlations for building envelope energy systems' modelling. *Appl Therm Eng* 28: 801–808. https://doi.org/10.1016/j.applthermaleng.2007.12.005
32. Woods L (1954) A note on the numerical solution of fourth order differential equations. *Aeronaut Q* 5: 176–184. https://doi.org/10.1017/s0001925900001177
33. Han J, Lu L, Yang H (2009) Thermal behavior of a novel type see-through glazing system with integrated PV cells. *Build Environ* 44: 2129–2136, https://doi.org/10.1016/j.buildenv.2009.03.003.
34. Rahman M, Hasanuzzaman M, Rahim N (2015) Effects of various parameters on PV-module power and efficiency. *Energy Convers Manage* 103: 348–358. https://doi.org/10.1016/j.enconman.2015.06.067
35. Akshayveer, Singh AP, Kumar A, et al. (2021) Effect of natural convection and thermal storage system on the electrical and thermal performance of a hybrid PV-T/PCM systems. *Materialstoday: Proc* 39: 1899–1904. https://doi.org/10.1016/j.matpr.2020.08.010
36. Alibakhsh K, Yasamin K, soudabeh G, et al. (2017) Effects of forced convection on the performance of a photovoltaic thermal system: An experimental study. *Exp Therm Fluid Sci* 85: 13–21. https://doi.org/10.1016/j.expthermflusci.2017.02.012

37. Saber B, Abderrahim B, Taqiy E, et al. (2024) Mixed convection air-cooled PV/T solar collector with integrate porous medium. *J Braz Soc Mech Sci Eng*, 46. https://doi.org/10.1007/s40430-024-04821-1
38. Nougbléga Y, Kpode K, N'Wuitcha K, et al. (2019) Thermal efficiency of a hybrid photovoltaic-thermal chimney integrated into a building. *Am J Mod Phys* 8: 50. https://doi.org/10.11648/j.ajmp.20190804.11
39. Nahar A, Hasanuzzaman M, Rahim N, et al. (2019) Numerical investigation on the effect of different parameters in enhancing heat transfer performance of photovoltaic thermal systems. *Renewable Energy* 132: 284–295. https://doi.org/10.1016/j.renene.2018.08.008
40. Ozueh T, Ajienka J, Joel O (2022) Exo-Economic analysis on the liquefaction unit of a baseload LNG plant. *Int J Adv Eng Manage (IJAEM)* 4: 1646. https://doi.org/10.35629/5252-040716461652
41. Tang J, Skelton J (2021) Impact of noble-gas filler atoms on the lattice thermal conductivity of CoSb3 skutterudites: First-principles modelling. *J Phys Condens Matter* 33: 15. https://doi.org/10.1088/1361-648X/abd8b8
42. Fonseca L, Miller F, Pfotenhauer J (2018) Experimental heat transfer analysis of a cryogenic nitrogen pulsating heat Pipe at various liquid fill ratios. *Appl Therm Eng* 130: 343–353. https://doi.org/10.1016/j.applthermaleng.2017.11.029
43. Betts P, Bokhari I (2000) Experiments on turbulent natural convection in an enclosed tall cavity. *Int J Heat Fluid Flow* 21: 675–683. https://doi.org/10.1016/S0142-727X(00)00033-3
44. Batchelor G (1954) Heat transfer by free convection across a closed cavity between vertical boundaries at different temperatures. *Q Appl Math* 12: 209–233. https://doi.org/10.1090/qam/64563

AIMS Press